RSC Sustainability

Accepted Manuscript

This article can be cited before page numbers have been issued, to do this please use: F. De Luca, P. Demoro, I. Nduka, C. Italiano, S. Abate and R. Arrigo, *RSC Sustain.*, 2025, DOI: 10.1039/D4SU00463A.

ROYAL SOCIETY OF CHEMISTRY

View Article Online
DOI: 10.1039/D4SU00463A

Carbon materials are increasingly important for their use in energy storage and conversion technologies. This is due to a tuneable surface chemistry and a high electrical conductivity, which make them ideal materials for hosting metal electroactive species. However, with the prospect of an increased use, carbon must be sourced sustainably. Waste biomass offers a sustainable alternative to fossil carbon and are abundantly available**.** Their reuse as raw materials for carbon manufacturing would reduce the impact of their disposal in the environment as well as associated costs. However, the structure of the C materials and the immobilised metal active species needs to be tailored to the specific technological application. At the same time, waste biomass, such as citrus waste are highly heterogeneous in nature and rich of active chemical constituents, with specific chemical properties. Thus the conversion of waste biomass into carbon-based materials requires an optimised synthetic protocol. In this study, the application of citrus waste is explored for the synthesis of electrocatalytic carbon-supported Cu nanostructured materials for CO_2 electrolysis to value added compounds. The CO_2 electroreduction reaction is of pivotal importance to produce C-based fuels sustainably.

Herein we advance the knowledge on how the biomass constituents as well as the Cu precursors interact during synthesis to yield electrocatalysts active in CO_2 reduction. We identify specific elements that lead to improved performances establishing direction in materials design starting from waste biomass. This work represents the first necessary step for the effective and sustainable reuse of waste biomass and aligns with the UN SDG 12, responsible consumption and production.

View Article Online
DOI: 10.1039/D4SU00463A

ARTICLE

Valorisation of Citrus Waste for Sustainable Synthesis of Carbon-Supported Copper Nanoparticles active in CO_2 Electroreduction

Received 00th January 20xx,
Accepted 00th January 20xx

DOI: 10.1039/x0xx00000x

Federica De Luca, [a] Palmarita Demoro, [a] Izuchica Nduka,[b] Cristina Italiano,[c] Salvatore Abate.[a*] Rosa Arrigo [b*]

This study describes a microwave-assisted hydrothermal method to synthesize carbon-supported Cu electrocatalysts for CO_2 conversion using citrus peels as both the carbon precursor and a reducing agent for Cu cations (chloride, nitrate, and sulphate). XPS, TEM, and XRD analyses reveal that the resulting Cu/Cu_2O core-shell nanoparticles are immobilized on or embedded within the carbon matrix, which is influenced by both the type of peel and the anions. The structural and functional differences between orange and lemon peel-derived catalysts stem from variations in the carbon matrix. Orange peel systems exhibit an optimal graphitic-to-defective carbon ratio resulting in a more balanced porosity, electron conduction, and Cu stabilization, leading to superior CO_2 reduction performance. Sulphate-based catalysts supported on orange-derived carbon showed optimal activity for CO and methane production due to their balanced structural properties. This work demonstrates the potential of orange peel waste as a sustainable feedstock for the production of CO_2 reduction electrocatalysts, offering a green strategy for waste valorisation and clean energy technologies.

Introduction

The remarkable versatility of carbon for various applications is due to its diverse dimensionality, structure and texture[1]. Properties such as a high surface area, tuneable surface chemistry, and a high electrical conductivity make carbon materials ideal candidates for hosting metal active species for various applications, including energy conversion and storage[2]. In CO_2 electroreduction by carbon-supported Cu-based nanoparticles (NPs), the choice of the carbon support influences significantly the product distribution.[3-5] The presence of in-plane vacancies on carbon supports as well as heteroatom doping[6-7] alter the electronic structure of the support itself and can induce specific interactions with immobilised metal active species. This, in turn, influences their behaviour towards adsorption and activation of CO_2 molecules, as well as the electron and proton tranfers.[8-9]. Copper nanoparticles supported on graphene have shown interesting activity and selectivity for CH_4 production, attributed to the participation of the support via hydrogen spill-over to the metal sites.[10] The selectivity towards ethylene was reported to increase when moving from single wall carbon nanotubes to reduced graphene oxide and onion-like carbon.[3-5] The enhanced performances of onion-like carbon in C-C coupling were attributed to the unique catalyst design, where the shell of onion-like carbon surrounding the Cu-based NPs was suggested to electro-reduce CO_2 to CO, thereby increasing the surface concentration of this on adjacent Cu NPs.[3] Waste biomass-derived carbon offers a sustainable alternative to fossil carbon (e.g. coal, charcoal) due to its inherent renewability and low cost[11,12]. The global agricultural waste production is estimated to reach 500 million tons per annum [13]. This vast quantity of underutilized resources represents a substantial and sustainable source of raw material. Additionally, reuse of waste streams reduces operational costs associated with waste disposal[14]. In a previous work,[15] we demonstrated that the choice of biomass as a feedstock for materials manufacturing is application-dependent and requires a rational approach for effective utilisation. This is due to the fact that biomass is rich in soluble chemical compounds that can be leveraged for the *in situ* generation of the metallic active species. Compared to impregnation and sol-immobilization methods, this approach enables a more extensive interaction of the solution based Cu species with the C-precursor during the simultaneous formation of both the graphitic C matrix and the metal NPs during synthesis, resulting in a composite material. This contrasts with impregnation methods, where interactions between the C and metal species are confined to the external surface or accessible porosity of the C particles. By exploring the use of citrus waste as a feedstock, we produced C-supported Cu-based-nanomaterials[16,17] in a one pot synthesis and we have demonstrated that citrus waste is two-fold advantageous: (i) it serves as the carbon support for copper NPs, and (ii) it provides the reducing compounds (e.g. ascorbic acid) required for the reduction of solution-based cationic copper species. Noteworthy, orange peel contains a large quantity of ascorbic acid as well as other epicatechin compounds,[15] which have yielded Cu-based electrocatalysts active in CO_2 electroreduction to value-added

[a] P. Demoro, F. De Luca, Dr. S. Abate
ERIC aisbl and CASPE/INSTM, Dpt. ChiBioFarAM
University of Messina
Viale F. Stagno D'Alcontres 31, Messina, 98166, Italy Address here.
[b] Dr. R. Arrigo, Dr. Izuchika Nduka,
School of Science, Engineering and Environment
University of Salford
M5 4WT, Manchester, UK
[c] Dr. Cristina Italiano
National Research Council of Italy (CNR-ITAE), Salita Santa Lucia Sopra Contesse 5, 98126, Messina, Italy
r.arrigo@salford.ac.uk
abates@unime.it

compound such as formic acid and oxalate. In this study, we further explore the one-pot microwave-assisted synthesis of carbon (C)-supported copper-based NPs with the aims to further enhance the performances of these electrocatalysts for CO_2 reduction reaction (CO_2RR). We use commercially available citrus peels (lemon and orange) and evaluate the influence of various copper precursors (sulphate, nitrate, chloride) on the structural characteristics of the supported NPs as a way to identify design strategies. We use microwave-assisted hydrothermal synthesis to reduce the synthesis time and achieve greater homogeneity in the temperature profile within the reactive mixture, compared to conventional heating. [18] We expect that the molecular level interaction between the peel carbonaceous matrix and the cationic and anionic species from the metal precursor solutions during synthesis will influence the topological and chemical characteristics of the synthetized materials offering an opportunity for fine-tuning of the performances[19-20]. This works aims to unveil these aspects with a comprehensive characterisation of the synthesized materials using scanning electron microscopy (SEM) for morphological analysis, X-ray photoelectron spectroscopy (XPS) for electronic structural analysis, and X-ray diffraction (XRD) and transmission electron microscopy (TEM) for structural characterization. Moreover, we use liquid chromatography-mass spectrometry (LC-MS) to characterize the nature of the chemical species extracted from the peels during the hydrothermal synthesis, offering valuable insights to help explain our results and optimize the synthesis process for better control and scalability. This in-depth structural analysis, in conjunction with the evaluation of the electrocatalysts performances, aims to identify promising avenues for the sustainable valorisation of biomass waste for the development of functional materials for energy applications.

Results and Discussion

The bulk and surface chemical compositions of the samples are summarized in Table 1. The surface abundance of copper exhibits minor variations depending on the copper precursor employed and remains relatively invariant irrespective of the citrus peel utilized. The T-$CuCl_2$-O sample presents the highest copper surface abundance of 5.30 wt%. The total copper content, as determined by energy-dispersive X-ray spectroscopy (EDS) is markedly higher than the surface abundance. For the samples with the highest copper loading, specifically T-$CuSO_4$-L, the overall content reaches 47.2%. The discrepancies between the overall bulk content and the surface content are due to the varying detection sensitivities of the two methods. XPS probes only the topmost layer, up to 10 nm in thickness, which means that the largest part of the particles is not detected, especially those within the pores of the carbon support. In contrast, these particles are the primary contributors to the EDS signal.

Table 1: a) XPS, and b) EDS elemental analysis (in weight %).

Sample	C	O	Cu	Cl	N	S
a) Surface elemental analysis						
T-$CuCl_2$-L	73.52 (±0.12%)	20.72 (±0.15%)	5.23 (±0.20%)	0.52 (±0.10%)	-	-
T-$CuCl_2$-O	77.52 (±0.13%)	16.18 (±0.16%)	5.30 (±0.20%)	1.01 (±0.10%)	-	-
T-$Cu(NO_3)_2$-L	80.53 (±0.1%)	13.81 (±0.1%)	3.34 (±0.20%)	-	2.31 (±0.19%)	-
T-$Cu(NO_3)_2$-O	77.75 (±0.14%)	17.07 (±0.18%)	3.45 (±0.21%)	-	1.73 (±0.21%)	-
T-$CuSO_4$-L	84.56 (±0.11%)	13.73 (±0.19%)	1.64 (±0.23%)	-	-	0.07 (±0.03%)
T-$CuSO_4$-O	79.95 (±0.14%)	15.67 (±0.15%)	3.45 (±0.24%)	-	-	0.93 (±0.15%)
b) Bulk elemental analysis						
T-$CuCl_2$-L	31.2 (±0.1%)	29.4 (±0.1%)	36.4 (±0.1%)	2.9 (±0.4%)	-	-
T-$CuCl_2$-O	35.5 (±0.1%)	31.3 (±0.1%)	33.2 (±0.1%)	-	-	-
T-$Cu(NO_3)_2$-L	31.4 (±0.1%)	31.2 (±0.1%)	30.3 (±0.1%)	-	6.7 (±0.2%)	0.4 (±0.5%)
T-$Cu(NO_3)_2$-O	28.9 (±0.1%)	31.3 (±0.1%)	34.5 (±0.1%)	-	4.7 (±0.2%)	0.5 (±0.5%)
T-$CuSO_4$-L	32.6 (±0.1%)	19.3 (±0.1%)	47.2 (±0.1%)	-	-	0.8 (±0.5)
T-$CuSO_4$-O	33.3 (± 0.1%)	24.1 (±0.1%)	41.4 (0.1%)	-	-	1.1 (±0.5%)

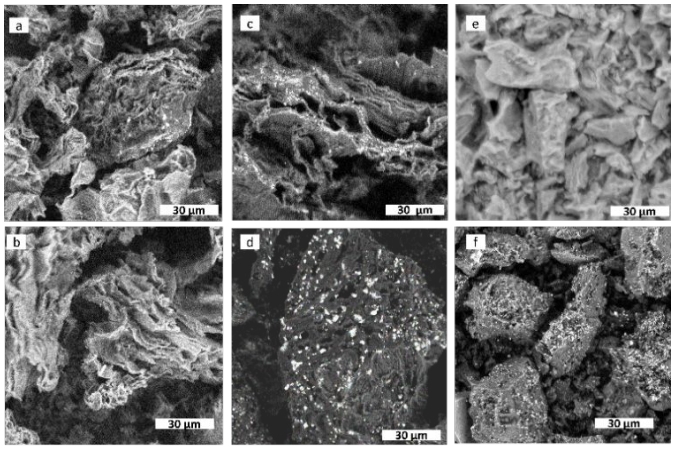

Figure 1: SEM images recorded with a Phenom ProX Desktop instrument at 10 kV acceleration voltage and at ×2000 magnification in back-scattered electron (BSE) mode: a) T-$CuSO_4$-O b) T-$CuSO_4$-L c) T-$CuCl_2$-O, d) T-$CuCl_2$-L, e) T-$Cu(NO_3)_2$-O, f) T-$Cu(NO_3)_2$-L.

Figure 1 (a, c and e) displays the back-scattered electron (BSE)-SEM images of the electrocatalysts supported on orange peel-derived carbon prepared using chloride, nitrate, and sulphate precursors, respectively. Figure 1 (b, d and f) shows the SEM images of the electrocatalysts prepared with the same precursors but supported on lemon peel-derived carbon. Accordingly, primary particles of the carbon supports are characterised by a flake-like morphology, consistent with a turbostratic structure characteristic of graphitic materials when there is disorder in the stacking of the layers. This stacking generates a hierarchical porous structure, highly heterogeneous in nature, in terms of pore size and shape. Moreover, the primary carbon particles are highly heterogeneous in size, with the nitrate-derived samples appearing to contain the smallest primary carbon particles. The contrast variations observed in the SEM images, where the brighter regions correspond to Cu-based NPs, indicate that these are located on the side edges of the C flakes and are larger for the chloride-derived samples, more so when supported on the lemon peel-derived system. The SEM image of the nitrate precursor sample shows Cu-based NP_S with the smallest particle size amongst the lemon peel-derived samples. The

differences in particle dispersion from the SEM images are more subtle for the orange peel-derived electrocatalysts.

X-ray diffraction (XRD) patterns of the synthesized materials are presented in Figure 2. Noteworthy, the samples exhibit characteristic diffraction peaks corresponding to crystalline Cu and Cu_2O, along with a broad peak attributed to the carbonaceous graphitic-like support. The diffraction peaks at 2θ values of about 43.3°, 50.34°, and 74.08° correspond to the crystallographic planes (111), (200), and (220) of metallic Cu[21], respectively (JCPDS no. 04-0836). Similarly, the peaks at 36.43° and 61.71° can be attributed to the (111) and (220) planes of Cu_2O (JCPDS no. 05-0667).[17] No additional crystalline phases were identified in the XRD patterns. Table 2 summarizes the sizes of the planes of the crystallites of the different phases.

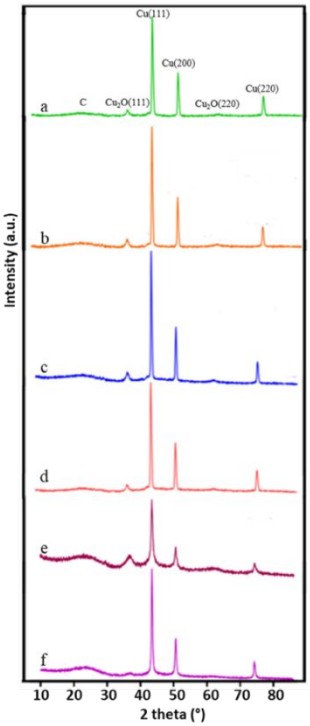

Figure 2: X-ray diffraction patterns of the as-prepared samples in the 2θ range of 10° to 85°. From top to bottom: a) T-$CuSO_4$-L, b) T-$CuSO_4$-O, c) T-$CuCl_2$-L, d) T-$CuCl_2$-O e) T-$Cu(NO_3)_2$-O, f) T-$Cu(NO_3)_2$-L.

Table 2: Crystallite size (nm) relating to each crystalline plane.

Sample	Cu_2O (111)	Cu^0 (111)	Cu^0 (200)	Cu_2O (220)	Cu^0 (220)
T-$CuCl_2$-L	13.2	23.1	21.6	11.3	20.9
T-$CuCl_2$-O	12.1	25.2	24.9	9.7	23.4
T-$(CuNO_3)_2$-L	9.0	19.2	20.7	15.6	9.4
T-$(CuNO_3)_2$-O	4.8	17.5	18.4	4.7	16.5
T-$CuSO_4$-L	7.5	19.6	20.3	7.7	23.1
T-$CuSO_4$-O	11.3	22.5	20.4	4.3	25.2

The analysis of the sizes of the different planes indicates larger metallic domains and smaller cuprous oxide domains when the chloride or sulphate precursors are used, more so for the orange peel-derived sample. The size variation of the different planes within the same phase further signifies morphological differences among the samples. When using the nitrate precursor, both Cu^0 and Cu_2O phases present comparatively the smallest crystallite size, consistent with the SEM analysis in Figure 1.

The TEM analysis provides further insights into the structural characteristics of the samples.

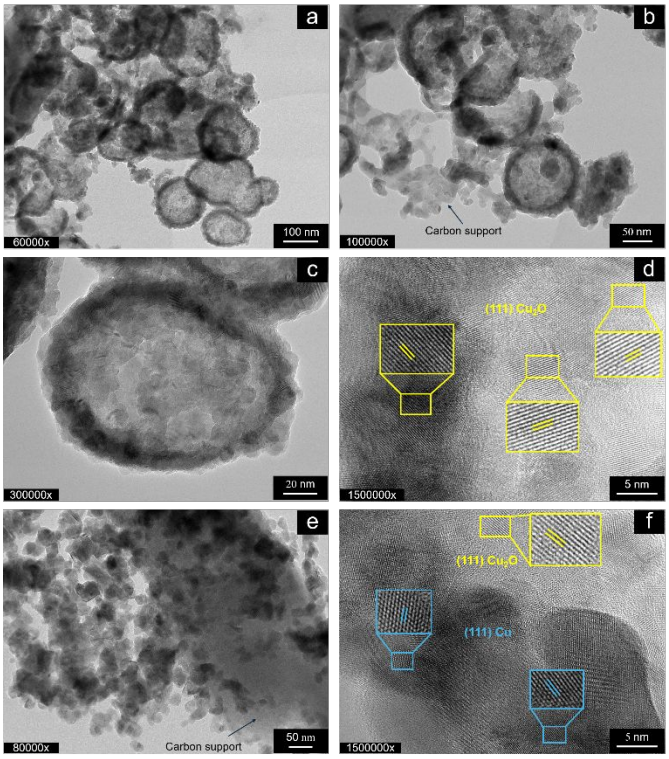

Figure 3: HR-TEM micrographs of as-prepared T-$CuSO_4$-O.

Figure 3 shows the TEM micrographs of the as-prepared T-$CuSO_4$-O at different magnifications. Carbon is dispersed throughout the sample, as indicated by the arrows in b and e. The Cu phase is composed of primary particles, which aggregate in a highly heterogeneous manner, forming rounded core-shell superstructures measuring approximately 100–200 nm in diameter (Figure 3a-d). These structures feature a less dense or voided core, while the Cu-based primary particles are concentrated in the shell. The size of the primary particles qualitatively aligns with the length of the crystalline planes determined by XRD. The core-shell particles exhibit lattice fringes spacing of 0.245 nm (Figure 3d), indexed to the mainly exposed (111) crystal planes of Cu_2O (JCPDS card no. 74-1230). In addition to the lattice fringes of Cu_2O, spherical agglomerates show lattice fringes spacing of 0.208 nm (Figure 3f), corresponding to (111) planes of metallic Cu (JCPDS card no. 01-1241). Figure 3e shows that in some areas primary particles are agglomerated with no specific order and decorate a carbon particle. Overall, these findings are consistent with the XRD analysis (Figure 2), providing a comprehensive understanding of the morphological characteristics of the sample. The TEM analysis of the samples derived from the

View Article Online
DOI: 10.1039/D4SU00463A

orange peel using Cu chloride and Cu nitrate as precursors are presented in Figure S1.

Cu chloride yields rounded particles of varying sizes, spanning one order of magnitude in lengths, most of which are voided core- shell particles (Figure S1a). The particles with a solid core are found mainly at the surface of the carbon support particle (Figure S1b), suggesting that the voided particles are embedded within the pores of the carbon support, with voids forming due to the kirkendall effect.[22] This contrasts with T-$CuSO_4$-O, which generally presents larger particles external to the carbon support. Figure S1b shows an example of a Cu-based NPs with ill-defined shape covering the carbon support, which exhibits graphite-like layers. The sample derived from cu nitrate shows particles decorating the flake-like carbon particle (Figure S1c), which are generally solid in the core, although smaller voided particles are also observed. These nanoparticles are much smaller for the nitrate-derived sample than in the previous cases, consistent with the SEM images in Figure 1. TEM analysis of lemon-peel derived samples is presented in Figure S2. The sulphate-derived sample (Figure S2a) shows the same characteristic particles, homogeneously distributed on the carbon

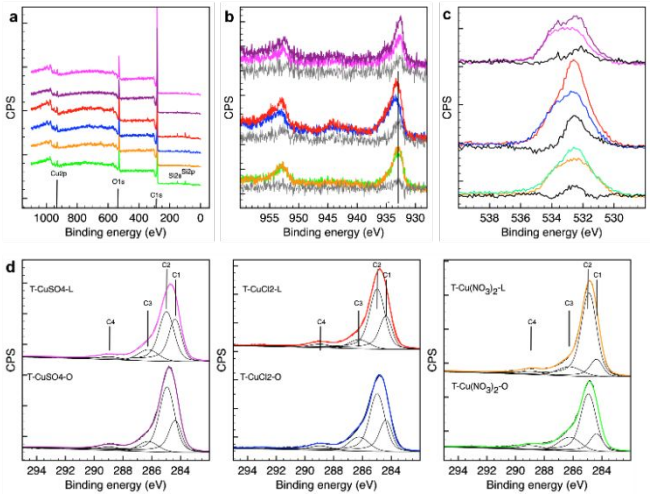

Figure 4: XPS analysis of the samples investigated using PHI VersaProbe II (Physical Electronics), equipped with an Al Kα (1486.6 eV) X-ray source. a) Survey spectra; b) Cu $2p_{3/2}$; c) O1s, and d) C1s. The colour code is consistent in this figure as follows: T-CuSO4-L (magenta), T-$CuSO_4$-O (purple), T-$CuCl_2$-L (red), T-$CuCl_2$-O (blue), T-$Cu(NO_3)_2$-L (orange), T-$Cu(NO_3)_2$-O (green).

support, with some voided particles and others featuring a metallic core with an oxide shell (Figure S2b). This sample differs significantly from T-$CuSO_4$-O, which shows unique morphological and structural characteristics in Cu speciation among the investigated samples, indicating a specific interplay between the nature of the peel and the Cu precursor during synthesis. In contrast, the chloride- and nitrate-derived samples exhibit Cu-based nanoparticles with nanostructural and morphological characteristics similar to their orange peel-derived counterparts, indicating that the peel plays a less significant role than the anion in determining the properties in these cases.

The electronic structure analysis of the fresh samples was investigated by XPS at the Cu2p, C1s, and O1s core levels (Figure 4).

The survey spectra in Figure 4a indicate a surface composition consisting of mostly C, O and Cu, with Si impurities observed in some cases.

The Cu2p XPS spectra (Figure 4b) show a subtle difference in Cu chemical speciation for the samples derived from nitrate precursor. The binding energy of the main $2p_{3/2}$ peak is found at 933 eV and no satellites features are present, indicating a reduced state of the catalysts. However, Cu^0 and Cu_2O are difficult to distinguish by Cu2p XPS, being the $Cu2p_{3/2}$ peak for these species at a very similar BE of 932.6 eV and 932.4 eV, respectively. The value found in this work falls well within the range reported for Cu/Cu_2O core-shell nanoparticles on thin C films (932.3 eV to 933.8 eV),[23] where the larger the metallic core and, the higher the Cu/C ratio, the lower the BE. A thin C overlayer on large Cu/Cu_2O sore-shell NPS would also give a similar BE shift.[15] Due to the surface sensitivity of the method, the XPS signal for these systems will be dominated by C overlayer/Cu-based NPs interphase region with a shift to lower values the thinner the C overlayer and the larger the metallic core. The samples prepared from a chloride precursor differ from the nitrate-derived samples in that they present a broader $Cu2p_{3/2}$ peak toward the higher BE side as well as the satellite peak, whose shape is consistent with Cu(II) hydroxide species. Moreover, the difference spectrum for the chloride samples shows a peak at approximately 932.4-932.6 eV, consistent with a larger contribution of metallic and Cu_2O species on the lemon peel-derived support. The results of the XRD analysis for these chloride-derived samples can be reconciled with the XPS findings by accounting for the different probing depths of the two techniques, where XRD provides bulk-sensitive information, reflecting the Cu phases throughout the sample volume including within the pores of the carbon support, whereas XPS provides the composition of the outermost layer. It is therefore possible to infer that T-$CuCl_2$-L presents regions with a thinner carbon (C) overlayer or more exposed NPs supported on the external surface, thereby allowing us to probe a larger portion of the metal-metal oxide NPs by XPS. The SEM image in Figure 1 shows that, compared to T-$CuCl_2$-O, a higher abundance of the Cu NPs are located on the external surface of T-$CuCl_2$-L, possibly due to the apparent lower porosity of this system.

The Cu2p spectra of the sulphate-derived samples are more similar to the nitrate samples in terms of Cu speciation, although some intensity around 935 eV suggests the existence of Cu(II) species in the former. We find that the orange support contains a higher abundance of a component centred at 932.5 eV, consistent with

View Article Online
DOI: 10.1039/D4SU00463A

larger portion of the Cu for this sample probed by XPS, thus a thinner C overlayer and/or more exposed Cu phases, consistent with TEM analysis (Figure 3). The XPS findings are also consistent with the XRD results and TEM analysis, indicating that the nitrate-derived samples exhibit the smallest particle sizes amongst the samples.

The O1s XPS spectra for all the samples present a broad peak ranging from 530 eV to 536 eV. From the difference spectra analysis of all the samples, one could identify at least three peaks centred at approximately 531 eV, 532.6 eV and 533.5 eV (Figure 4c). The O species due to the Cu_2O are generally found at a lower BE [24] and therefore it is possible to infer that the O1s spectrum is dominated by the O species on the C support. Noteworthy, whilst the O1s profile for the orange-peel derived samples is very similar, regardless of the metal precursor used, a large variation is observed for the lemon peel-derived materials. A closer inspection indicates that the nitrate-derived sample on the orange peel support contains a larger abundance of a component centred at 532.6 eV BE than on the lemon peel support, which is assigned to C-O species[25]. T-$CuCl_2$-O is also characterised by higher abundance of more oxidised C-O species as evidenced by the components at higher BE. For the sulphate systems, T-$CuSO_4$-O presents higher abundance of a component at approximately 532 eV, which are either more reduced C-O species, or Cu(II)-bound oxygen species. Amongst the lemon-peel systems, the sample produced from the chloride precursor presents higher abundance of a component at approximately 532 eV together with a species at 531 eV which can be attributed to the Cu(II)-bound OH species, consistent with more exposed Cu-phases.

The analysis of the C1s XPS spectra provides more insights into the influence of the metal salt precursor on the graphitization process of the support during the thermal treatment. The spectra were fitted using a model develop earlier[26,27] which includes the following components: C1, 284.35 ± 0.01; C2, 284.90 ± 0.01; C3, 286.20 ± 0.01; C4, 288.80 ± 0. 01. C1 is assigned to sp^2 graphitic C; C2 is attributed to highly disordered graphite due to heteroatoms, with large contribution from C in a sp^3 bonding configuration; C3 is attributed to C–O species in cellulose[28] and is expected to convert first into C2 and then into C1 as the structure reorders upon thermal annealing. C4 is due to carbonates.[27] T-$CuSO_4$-L present the highest graphitic character among the samples. This is in contrast with a previous work[15], in which the metal loading was significantly lower as a result of a different reactive condition realised in a stirred reactor, suggesting an important role of the metal species in the deoxygenation reaction of the peel taking place during the hydrothermal synthesis as well as the subsequent thermal treatment. T-$CuSO_4$-O contains higher abundance of disordered graphite (C2) than T-$CuSO_4$-L, but also a slightly higher amount of the C-O component from the starting peel precursor. A striking difference is observed for the samples from nitrate precursor, which present the lowest graphitic character, regardless of the starting peel. This can be explained by the oxidative action of the nitrate species during the hydrothermal synthesis, which, by introducing oxygenated functionalities on the C backbone of the insoluble peel

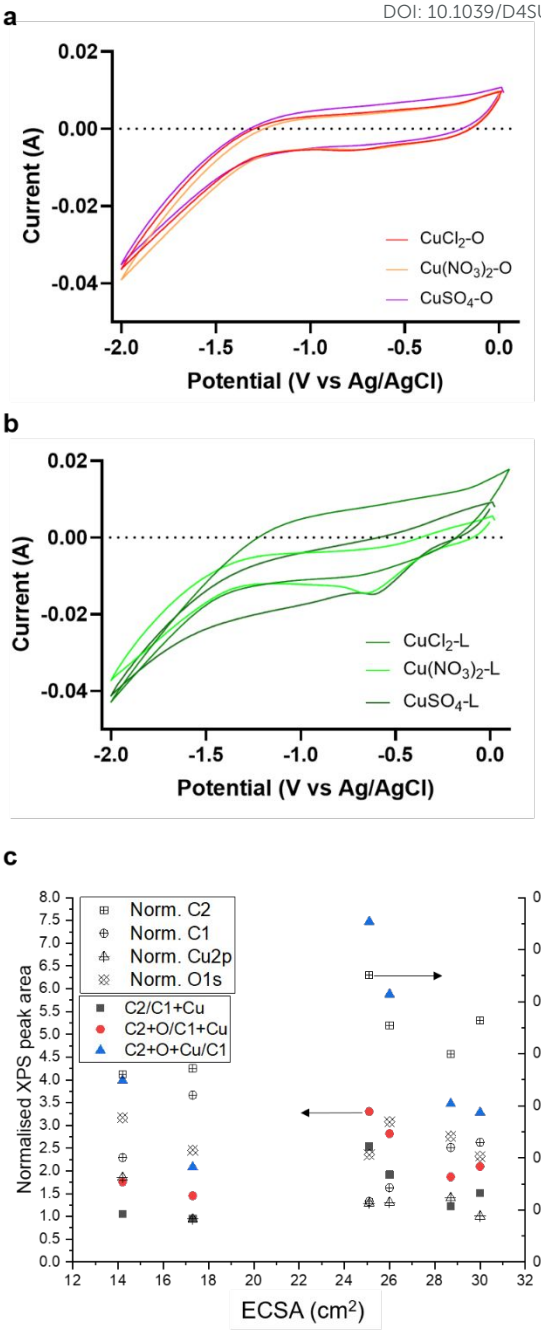

Figure 5: Cyclic voltammetry of lemon supported (a), and orange supported (b) electrodes in 0.1M $KHCO_3$ CO_2-saturated solution. (c) Correlative analysis XPS data vs. ECSA. White symbols are related to the abundance of the elements as indicated obtained normalising the relevant peak area by the sum of the peak areas of the C, O and Cu core levels. Coloured symbols are related to peak area ratios of the core levels (or in the case of the C core level also individual component derived from the fitting, namely C1 and C2) according to the formulas indicated in the legend.

constituents, contrasts the condensation/dehydrogenation reactions which are a necessary step to form condensed aromatic ring. It is interesting to note these results qualitatively correlate with the thickness and lengths of the flakes stacking in the C particles seen

View Article Online
DOI: 10.1039/D4SU00167A

in the SEM images in Figure 1 and in the TEM images in Figures S1 and S2. Accordingly, the nitrate-derived samples exhibit smaller carbon particles, and consequently smaller graphitic domains.

Moreover, a higher degree of graphitization is found together with larger Cu^0 and Cu_2O coherent domains (Table 2), which result from thermally induced particle growth, alongside some oxidised Cu(II) species, suggesting the presence of exposed and unprotected particles. In contrast, smaller particles are found for a more disordered C structure, indicating a stronger interaction between the Cu species and the carbon support matrix during the synthesis. Therefore, it is possible to infer that not only the chemical composition of the peel as earlier discovered,[15] but also the nature of the anion influences the reducibility of the Cu species by the peel constituents, as well as the transformation of the peel itself during thermal treatment. From the TEM analysis, it is possible to deduce that during the hydrothermal synthesis, some of the particles are directly formed within the pores of the peel solid component, which undergoes restructuring influenced by the metal species as discussed earlier. This phenomenon is particularly evident in the lemon-peel-derived samples**.** The similarity of particles nanostructures derived from the same Cu precursor, regardless of the peel type, indicates that the migration of soluble, solvated anion-bound Cu species into the pores of the insoluble peel component is influenced by the anion size. Smaller anions, such as NO_3^- (179 pm), can access smaller pores, leading to the formation of smaller particles. In contrast, larger anions like Cl^- (184 pm) and SO_4^{2-} (258 pm) preferentially migrate into larger pores, resulting in higher Cu concentration in these regions. In smaller pores, lower Cu concentrations leads to the formation of voided particles through kinkerdall effect.[22] However, it is also important to consider that particle formation can occur in solution due to the action of molecular or oligomeric constituents derived from the original peel. This phenomenon explains the presence of agglomerated solid-core particles deposited on the solid peel components without intimate interactions with them. These are the predominant form of Cu nanostructures in T-$CuSO_4$-O, consistent with the larger anion size and increased extraction process of the constituents during the hydrothermal synthesis. In order to understand the nature of the species released into the solution, we used liquid chromatography mass spectrometry. We analysed the liquid phase of the suspension after the simulated hydrothermal treatment of the peel at the same pH of the synthesis but without the Cu precursor (Figure S3). Accordingly, the solutions from both peels contain a large variety of chemicals of similar nature. The most notable difference between the peels is that orange peel releases certain chemicals not detected in the case of the lemon peel. Peaks corresponding to masses of 580 m/z and 610 m/z are assigned to Narirutin and Hesperidin, respectively. Additional peaks with masses of 372, 402, and 432 m/z are consistent with Sinensetin or Tangeretin, Hexamethoxyflavones (e.g., Nobiletin), and Heptamethoxyflavones (e.g., Methoxynobiletin), respectively.[29] It is their antioxidant ability that facilitates the reduction of ligated-Cu(II) species in the bulk of the solution, leading to its deposition on the insoluble constituents. To explain the formation of large spherical supra-structures, it seems logical to consider oligomeric species in the suspension acting as a template for the Cu supra-structures. To summarize, we can distinguish between insoluble peel-mediated nucleation and growth of Cu-based particles and a solution-based particles nucleation and growth. The former leading to particles within the pores, whereas the latter one leading to exposed NPs

The electrochemical behaviour of the samples was investigated using cyclic voltammetry (CV), (Figure 5), within the potential range 0 ÷ -2 V vs Ag/AgCl, to elucidate their redox properties.

The CV profiles revealed a reduction peak at approximately -0.86 V vs. the Ag/AgCl reference electrode (Eq. 1). This peak can be attributed to the one-electron reduction of Cu^+ to Cu^0, as described by the following equation

$$Cu^+ + H^+ + e^- \rightarrow Cu^0 \qquad \text{(eq. 1)}$$

and confirms exposure of the Cu nanostructures to the electrolyte solution. Furthermore, the onset of hydrogen evolution reaction (HER) was observed around -1.37 and 1.26 V vs. Ag/AgCl for lemon and orange peel system, respectively. The CV profiles of the orange-peel derived samples are notably similar, which aligns with the fact that the Cu and O speciation observed in the XPS analysis (Figure 3 b and C) for these samples are rather similar. These elements are the primary contributors to the capacitive behaviour of the samples. In contrast, the CV of the lemon peel-derived samples differ significantly, with the T-$CuCl_2$-L presenting the largest capacitive behaviour consistent with the highest O abundance (Table 1). The electrochemically active surface area (ECSA) of the synthesized materials was estimated using the method outlined by Qiao *et al.*[30]. In electrocatalysis, ECSA is a more relevant parameter than BET surface area because it quantifies the portion of the material accessible to the electrolyte ions. Higher ECSA generally translates into more sites for reactant adsorption, electron transfer, and product desorption, potentially leading to enhanced electrocatalytic performance[31]. The calculated ECSA values are summarized in Table 3. Noteworthy, samples supported on orange peel consistently exhibited higher ECSA compared to those supported on lemon peel. The ECSA values for the orange peel-supported catalysts follow the trend: T-$CuSO_4$-O ≥ T-$CuCl_2$-O > T-$Cu(NO_3)_2$-O. The ECSA values for the lemon peel-supported catalysts follow the trend: T-$Cu(NO_3)_2$-L > T-$CuSO_4$-L > T-$CuCl_2$-L. Intuitively, higher ECSA could be attributed to the larger exposed metal surface area, higher metal dispersion and the increased hydrophilicity due to the high C-O content in the C matrix of these samples.

Table 3: Calculated electrochemical active surface area (ECSA) of each thermally treated sample.

Sample	ECSA (cm^2)
T-$CuCl_2$-L	14.2
T-$CuCl_2$-O	28.7
T-$(CuNO_3)_2$-L	25.1
T-$(CuNO_3)_2$-O	26.0
T-$CuSO_4$-L	17.3
T-$CuSO_4$-O	30.0

View Article Online DOI: 10.1039/D4SU00463A

Table 4: Summary of faradaic efficiencies (FE) to formic acid (FA), carbon monoxide (CO), and methane (CH_4), and average current density (J) of samples.

Sample	FE_{FA} (%)	FE_{CO} (%)	FE_{CH4} (%)	J (mA/cm^2)
-1.8 V vs Ag/AgCl				
T-$CuCl_2$-L	7.5 (±1.0)	-	-	-1.07
T-$CuCl_2$-O	3.6 (±0.5)	8.0 (±1.2)	-	-3.08
T-$(CuNO_3)_2$-L	4.0 (±0.5)	-	-	-1.90
T-$(CuNO_3)_2$-O	2.0 (±0.3)	6.5 (±0.8)	-	-3.10
T-$CuSO_4$-L	1.1 (±0.2)	-	-	-3.00
T-$CuSO_4$-O	5.0 (±0.7)	8.7 (±0.4)	-	-2.90
-2 V vs Ag/AgCl				
T-$CuCl_2$-L	2.5 (±0.5)	-	-	-1.11
T-$CuCl_2$-O	1.3 (±0.2)	12 (±1.3)	4 (±1)	-4.35
T-$(CuNO_3)_2$-L	1.3 (±0.5)	-	-	-3.83
T-$(CuNO_3)_2$-O	2.4 (±0.6)	10 (±0.9)	1.8 (±0.5)	-4.10
T-$CuSO_4$-L	1.3 (±0.5)	-	-	-3.80
T-$CuSO_4$-O	1.6 (±0.5)	12.8 (±0.8)	4 (±0.5)	-4.00

Another important aspect to consider is that the higher graphitic disorder in these samples leads to an increased porosity (SEM images in Figure 1). Figure 5c presents an attempt to correlate the chemical composition of the electrocatalysts as determined by XPS with the corresponding ESCA values. We focus on the relationships between the ESCA value and the abundance of the C1 component (ordered sp^2 C), the C2 component (disordered sp^2-sp^3 C), the total surface Cu abundance and the total surface O abundance as determined by XPS. It is evident that there is not a clear trend between the ESCA values and the abundance of the different core levels, indicating a more complex interdependence. Moreover, the assumption that the porosity, is represented by the C2 component (disordered sp^2-sp^3 C) over the C1 component (ordered sp^2 C), and that the additive contribution of O species and Cu species determine the ESCA, is not consistent with the experimental values (blue triangles data in Figure 5c). However, the data suggests that high ESCA values are obtained with high C2 value, where the highest ESCA is obtained with an intermediate abundance of the graphitic peak. It follows that the C1 component plays a dual role, having an opposing effect on the ESCA value, which requires an optimal composition of the carbon matrix. On the one hand, a higher abundance of C1 may indicate reduced porosity; on the other hand it ensures good electron conduction which is paramount for electrocatalysis. Additionally, we analysed the abundance of Cu and O species as additive, direct, or inverse contributions to the ESCA value and found that they have only a minor effect on these correlations (as seen by the similar trends of the data points indicated by red circles and black square in Figure 5c). This suggests that not only the textural properties of the C matrix but also its electronic structural characteristics influence the ECSA value. This is consistent with a recent work on structural disorder and how this determines capacitance in nanoporous carbons.[32]

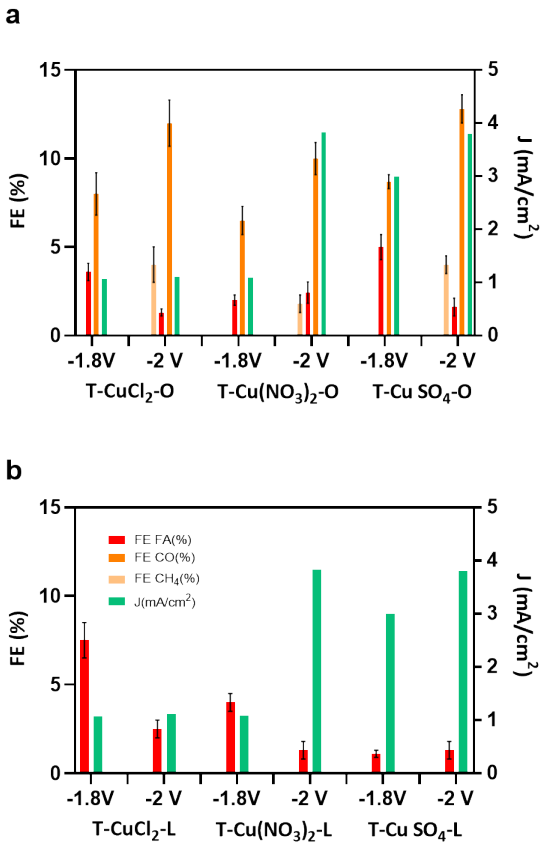

Figure 6: Current density (J), and faradaic efficiency of formic acid (FA) and Carbon monoxide (CO) and methane (CH_4) of a) orange peel-derived samples, and b) lemon peel derived sample after 1 hours of testing at an applied potential of -1.8 and -2 V vs Ag/AgCl.

Next, we discuss the electrocatalytic performances of these systems in CO_2RR. In this work, we focus on $KHCO_3$ as the electrolyte, rather than KOH,[15] because the lower pH favours multi-electron transfer in CO_2RR[33]. Moreover, in a previous work, the use of KOH as the electrolyte led to the formation of carbonates near the catalyst surface causing catalysts passivation. [34] The electrocatalytic tests in a CO_2-saturated 0.1 M $KHCO_3$ electrolyte under potentiostatic conditions were performed using a previously described custom-made three-electrode electrochemical cell.[35] The CO_2RR performance was evaluated over a 1-hour timeframe at applied potentials of -1.8 V and -2.0 V vs. Ag/AgCl reference electrode. The data are summarized in Figure 6 and Tables 4.

The selectivity of the electrocatalyst, that is its ability to favor CO_2RR over HER, is a crucial parameter for its performance. The observed product distribution appears to be strongly influenced by the support material. As shown in Figure 6 and Table 4, electrocatalysts derived from lemon peel primarily produced formic acid (FA) at both applied potentials with the highest faradaic efficiency (FE) for FA production, reaching approximately 7.5% for T-$CuCl_2$-L at -1.8 V vs Ag/AgCl, whilst

View Article Online
DOI: 10.1039/D4SU00463A

the performance deteriorate at more negative potential. Conversely, the orange peel-derived catalysts exhibited a more diverse product distribution, including FA, CO, and at more negative potentials also CH_4. T-$CuSO_4$-O reached the greatest FE of CO, CH_4 around 12.8 %, and 4%, respectively. The trend that emerges from Figure 6 and Table 4 is as follows: the sum of FEs increases in the order T-$Cu(NO_3)_2$-O < T-$CuCl_2$-O < T-$CuSO_4$-O, consistent with the trend observed for ECSA. The observed differences in product selectivity might be attributed to different factors, all accounting for the chemical properties of the original peel and how this influences the structure of the resulting electrocatalyst. The importance of the nanostructure of the C support was already evidenced earlier[15], where the further annealing of the Cu electrocatalysts up to 800 °C resulted in a deterioration of the electrocatalytic performances, suggesting that the optimal balance between ordered sp^2 C, needed for electron conduction, and defective sp^3 carbon was an important aspect. In the present work, we are able to clarify the role of these defective C, which leads to an increase in the ECSA by introducing not only porosity but also optimal electron conduction, thereby resulting in improved performances. The ECSA value is proportionally relatable to the current density; however it is insufficient to ensure high selectivity to CO_2 reduction product, particularly to multi-electron transfer products such as methane. One such example is the T-$Cu(NO_3)_2$-L having a relatively high ECSA, comparable to the orange-peel derived systems, but yielding FA at -2 V vs Ag/AgCl with a relatively low FE of approximately 1.7 %, despite the high current density observed. Therefore other aspects beside the ECSA value need to be considered to explain the selectivity issue. A role played by the peel constituents concerns the influence on the Cu phase at the nanoscale, through the interactions of the insoluble cellulosic part with the Cu species in solution as well as the capping properties of the molecular constituents of the peel as the NP_S are formed under hydrothermal conditions. These phenomena will influence the size of crystallographic planes of the Cu nanostructures (Figure 2) and the electronic structure (Figure 4b) as we al the location of the particles within the C matric, thus the exposure of the Cu phases (Figure 1 and 3).

In Figure 7, we attempt to establish a correlation between the product selectivity and the structural features related to the metal phase. It is important to note that these correlations, which are based on the initial state of the electrocatalyst will not provide a direct information about the nature of the active state, but rather of a precursor state, which will convert into the active state under CO_2RR condition. The nature of the active Cu state has been extensively studied using advanced experimental and computational methods, with contrasting observations regarding its influence on selectivity, making it an ongoing topic of debate.[36-37] However, a recurring observation has led to the hypothesis that a mixed Cu/Cu_2O phase is crucial for selective CO_2 electrocatalysis.[38] The transformation of Cu electrocatalysts into an ordered Cu(111) phase under cathodic potentials, driven by thermodynamics, is indeed detrimental for CO_2 electrocatalysis.[39] Therefore, the first step in materials design is to explore how to kinetically stabilize this mixed phase. In this work, the strategy involves entrapping the Cu phase within the C matrix. Thus, the analysis presented here can be considered an assessment of the readiness of the precursor state for selective electrocatalysis.

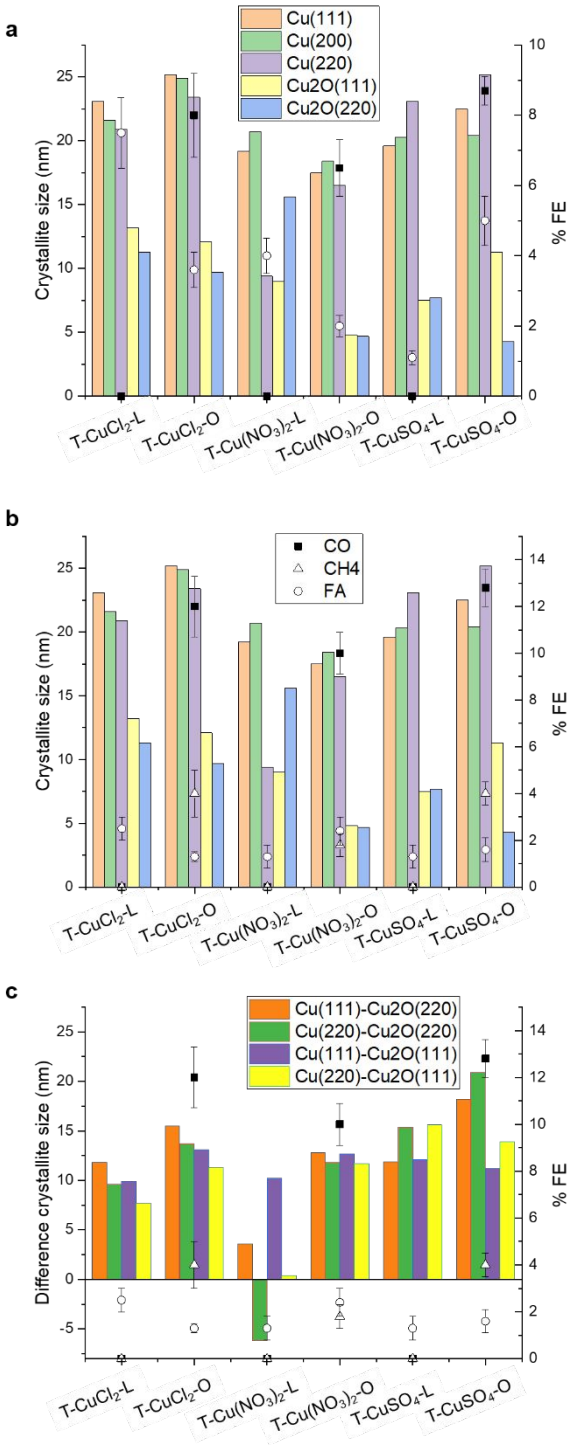

Figure 7: (a) Correlation between the FE obtained at -1.8 V vs Ag/AgCl and the size of the planes as indicated, determined by XRD analysis; (b) Correlation between the FE obtained at -2 V vs Ag/AgCl and the size of the planes as indicated, determined by XRD analysis; (c) Correlation between the FE obtained at -2 V vs Ag/AgCl and the difference between the size of the planes as indicated.

From Figure 7a and b, it is evident that there is not a linear correlation of the %FE with any of the individual crystallographic

View Article Online DOI: 10.1039/D4SU00463A

components in the initial state of the electrocatalysts. We suggest that this is due to the exposure of the Cu phases contained in each electrocatalysts and how these transform *in situ* differently during CO_2RR due to a specific localization and stabilization within the C matrix. This is not surprising as it is well known from mechanistic studies using advanced theoretical and experimental approaches that many factors influence the catalytic performances in a complex interdependency, including surface nanostructure and composition,[40] mesoscale structural and textural characteristic,[41] reactions conditions (pH, buffer strength, ion effects),[42] mass transport related effects,[43] and local electric or magnetic field.[44] All these aspect would influence the availabilities of reagents and active sites dynamics at the polarized interface. A limitation in assessing a structure activity/performance is the fact that the exposed metal active phase remains unknown for these partially encapsulated particles, but the selectivity issue can be discussed. Based on these results, we suggest that the apparent condition for achieving higher CO_2RR faraday efficiency for the formation of multi-electron reduction product is a higher Cu^0/Cu_2O ratio, regardless of the absolute value of the crystallite size, whereas larger Cu_2O crystallites favor FA formation. From Figure 7c, it seems that in the case of the orange peel-derived samples, the higher the difference in crystallite size between the metallic and cuprous oxide planes, namely Cu(111) - Cu_2O(220) and Cu(220) - Cu_2O(220), the higher the total CO_2RR faraday efficiency as well as the FE towards methane at 2 V vs. Ag/AgCl. This correlation could be explained in terms of an optimal co-location of Cu_2O/Cu planes, where the Cu(I)-Cu(0) sites at the interface are involved in the activation of CO_2 and the metallic planes provides the H^+ and e^- needed for the hydrogenation reaction. [45]

The pores generated by the turbostraticity of the layers offer an avenue for particles stabilization. We observed that the particles are interacting at the edges sides of the bent graphite flakes (Figure 1), were the bending causes charge localization leading to an increased stabilization of nanoparticles at the edge sites [46]. The presence of a carbon overlayer could be also a crucial aspect in the stabilization of the CO_2RR active and selective phase, aligned with the well-established role of the carbon overlayer in regulating selectivity for metal nanoparticles in heterogeneous catalysis[47]. However, the nature of the carbon component—whether as the support interacting with Cu phases or as the carbon overlayer on Cu phases—can also be expected to influence electrocatalysis.

For the lemon peel-derived systems, no clear correlation has been observed between the initial Cu phases and CO_2 reduction reaction (CO_2RR) performance at -2 V vs Ag/AgCl. Similarly, there is no evident correlation with the electrochemical surface area (ESCA), and thus with the textural and electronic properties of the support. The results on the lemon peel samples are consistent with the high FA efficiency observed for reduced graphene oxide (rGO)-supported Cu nanoparticles, and attributed to oxygenated groups in rGO, limiting the electron transfer process. [48]We postulate that the performances are dominated by the electrochemical properties of the support, together with an exposed Cu phase predominantly as Cu_2O. Additionally, the exposed Cu_2O phase may lack the stabilizing effect of the pores, leading to its rapid transformation under reaction conditions into a metallic Cu system selective for HER. TEM images reveal that most particles are embedded within the carbon matrix, rendering them inaccessible for catalysis. This finding implies a crucial role for the structural attributes of the carbon support in influencing product formation and selectivity, which depend on the choice of the biomass as well as the metal precursor.

Conclusions

This study explored the role of the copper precursors, specifically chloride, nitrate and sulphate, in the synthesis of C-supported Cu-based electrocatalysts active in the CO_2RR. During the hydrothermal synthesis, the combined redox properties of the peel constituents, along with the redox properties of the counter anions (Cl^-, NO_3^-, SO_4^{2-}) control the thermally induced restructuring and graphitization of the insoluble peel constituents, generating intrinsic porosity. The cumulative effect of the redox properties of the peel constituents and the nature of the anion will also determines the surface oxygenated moieties on the insoluble part, which act as anchoring sites for the metal nanoparticles, thereby influencing their location within the structure. At the same time, the molecular constituents of the peel facilitate the formation of Cu_2O/Cu particles through their reducing and capping properties.

The particle distribution within the C matrix indicates that counter anion affects the final particle location, with the sulphate anion favouring the formation of particles on the external surface of the support. Consequently, the sulphate precursor produces an electrocatalyst with a higher FE for CO_2 reduction products, including multi-electron reduction products like methane. However, the nature of the starting peel plays a major role in determining performances. Electrocatalysts derived from the orange peel- exhibited superior characteristics compared to those synthesized using lemon peels. Orange peel-derived samples resulted in the formation of larger metallic domains in the Cu_2O/Cu nanoparticles and an optimised structural composition of the C support, in terms of sp^2 and sp^3 character, which ensured electron conduction and porosity, respectively.

This optimization enhanced the electrochemically active surface area (ECSA) and promoted a diverse CO_2 reduction product distribution, including CO, CH_4, and formic acid.

Notably, the T-$CuSO_4$-O catalyst achieved the highest faradaic efficiency for both CO (12.8%) and CH_4 (4%) production at −2 V vs. Ag/AgCl. In contrast, lemon peel-supported catalysts primarily produced formic acid regardless of ECSA value, indicating limited interfacial electron transfer, characteristic of a performance dominated by the carbon support. Additionally, excessive copper exposure might induce phase transformations favouring the competing hydrogen evolution reaction.

Overall, this work highlights the potential of valorising citrus waste, particularly orange peels, to produce efficient CO_2 reduction electrocatalysts. These findings encourage further exploration of waste biomass sources for developing advanced

View Article Online
DOI: 10.1039/D4SU00467A

electrocatalysts. While this study focused on CO_2 electrocatalytic conversion, the chemistry unveiled is also relevant to other clean energy applications.

Experimental Section

Synthesis of Cu catalyst samples: In our synthetic protocol, 18 mmol of the Cu salt ($CuSO_4$ anhydrous powder, 99.99 % purity from Sigma Aldrich; $Cu(NO_3)_2$, hydrate powder, 99.999% Sigma Aldrich; $CuCl_2$ anhydrous powder 99%, Sigma Aldrich) was dissolved in 30 mL of distilled water at 50° C for 10 minutes. Two commercial citrus peels from Nutripowder were used, namely the orange peel and the lemon peel. 0.65 g of finely grinded citrus peel powder, either from lemon or orange, was suspended in 4 mL of the Cu precursor solution and diluted to 8 mL with distilled water in a 10 mL microwave tube, thus irradiated at 68 °C for 11 minutes under continuous stirring using a CEM Discover SP Microwave Reactor. The suspension was allowed to cool for 2 minutes and centrifuged at 1500 rpm for 8 minutes. The solid material was washed with distilled water and ethanol, vacuum filtered and used for further analyses and testing. The samples notations are listed in the table 5.

Table 5: Synthesized electrocatalysts and their characteristics.

ID sample	Description
T-CuCl-L	500°C -Precursor-Lemon
T-CuCl-O	500°C- Precursor-Orange
T-$Cu(NO_3)_2$-L	500°C -Precursor-Lemon
T-$Cu(NO_3)_2$-O	500°C- Precursor-Orange
T-$CuSO_4$-L	500°C -Precursor-Lemon
T-$CuSO_4$-O	500°C- Precursor-Orange

Electrode preparation: The synthesized catalysts underwent thermal treatment in an argon atmosphere. This involved heating them to 500 °C for 2 hours with a controlled temperature ramp of 5 °C per minute. Following thermal activation, an ink was prepared for fabricating the working electrode. This was achieved by dispersing 8 mg of the catalyst (corresponding to a loading of 0.5 mg/cm²) within a mixture containing 20 µL of a 10 wt% Nafion solution (Aldrich) and 1.1 mL of anhydrous absolute ethanol (Carlo Erba). The mixture was then sonicated for 2 hours to ensure homogeneous distribution of the catalyst particles throughout the ink. The prepared catalyst ink was then deposited onto a SIGRACET GDL 28 BC gas diffusion layer with a geometric surface area of approximately 16 cm² using a spray coating technique.

Electrocatalytic test: This study investigated the electrochemical conversion of CO_2 into liquid products using a two-compartment cell separated by a Nafion® 115 cation exchange membrane. The working electrode (WE) was comprised of thermally treated samples with a geometric surface area of approximately 6 cm². A 0.1 M $KHCO_3$ solution saturated with CO_2 was employed in the cathodic compartment, while the anodic compartment contained a 0.1 M $KHCO_3$ electrolyte solution. CO_2 gas (20 ml/min) was flowed through the cathode tank for 20 minutes to ensure saturation of the electrolytic solution. A peristaltic pump circulated the electrolyte solutions between the compartments. The total solution volume (cathode + external tank + tubes) was 35 ml, with each compartment holding 7 ml. Amperometric detection experiments were conducted at constant applied voltages ranging from -1.8 V to -2 V vs. Ag/AgCl, with current density being monitored. In the anodic compartment, water co-electrolysis produced protons (H^+) in situ. These protons migrated through the Nafion membrane towards the cathode where the CO_2 reduction reaction occurred. The tests were carried out for two hours at each investigated potential. Liquid products were analysed using ion chromatography with a mobile phase of 0.05 mM H_2SO_4, a flow rate of 0.05 ml/min, and a pressure of 5 MPa. The stationary phase consisted of a 25 cm organic acid column with a 7.8 mm internal diameter preceded by a 50 mm x 4 mm Metrosep Organic Acid Guard pre-column. A 944 professional UV/vis detector with a wavelength of 215 nm was used for product detection. Gaseous products accumulating in the headspace were analysed using an online micro gas chromatograph (Micro GC, Agilent 490) equipped with two columns: (i) PoraPLOT Q for volatile organic compounds and (ii) Molsieve 5A for separating inorganic compounds (H_2, N_2, O_2, CO, and CH_4). A thermal conductivity detector (TCD) was employed for analyte determination. Faraday efficiency is calculated following the eq. 2.

$$FE = (\alpha * n * F)/Q \quad \text{(eq. 2)}$$

where α is the number of electrons transferred n is the number of moles of the product yielded; F is the Faraday's constant (96485 C.mol-1); Q is the average charge passed.

Cyclic voltammetry (CV): Cyclic voltammetry in the potential range 0÷-2 V vs Ag/AgCl and scan rate of 50 mV/sec was carried out in 0.1M $KHCO_3$ solution saturated with CO_2.

Electrochemical active surface area (ECSA): Cyclic voltammetry is employed to estimate the electrochemically active surface area of the samples. The initial step involves determining the double-layer capacitance (C_{DL}). To achieve this via CV, measurements were recorded at various scan rates within a non-faradaic potential window, as reported by Connor et al. [31]. The sample in table 1 were used as working electrodes for recording CVs in a N_2-saturated 0.1 M $NaClO_4$ solution. The chosen non-faradaic potential range extends from 0.05 V to -0.35 V vs. Ag/AgCl, employing scan rates of 10, 20, 50, 80, and 120 mV/s. The formula presented in eq. 3 was used to calculate the C_{DL}

$$I=C_{DL}*v \quad \text{(eq. 3)}$$

The linear relationship between the two parameters makes easy to assess the CDL value. It is calculated by taking the absolute value of the slope of the regressed straight lines[49]. Once determined the value of the C_{DL}, ECSA was calculated according to eq. 4[50]

$$ECSA=C_{DL}/C_s \quad \text{(eq. 4)}$$

C_s is the specific capacitance and in these used conditions is equal to 30 μF[51].

Measure of crystallite: The Scherrer equation (eq. 5) was employed to calculate the crystallite sizes based on the obtained diffraction data.

$$\tau=(K\lambda)/\beta\cos\theta \quad \text{(eq. 5)}$$

where τ is the average size of the ordered crystalline; K is a dimensionless shape factor (close to the unity); λ is the X-ray wavelength; β is the line that widens to half the maximum intensity; θ is the Bragg's angle.

Characterization

High-resolution transmission electron microscopy (HR-TEM) images were obtained using a cold field transmission electron microscope (JEM-F200, Jeol, Japan).
The morphology of the thermally treated samples was investigated using a Phenom ProX Desktop SEM instrument.
The crystallographic phases were identified using a Bruker D8-Advance X-ray diffractometer (XRD) with Cu-Kα radiation (λ = 1.54186 Å).
LC-MS analyses were performed using a Waters Acquity Premier UPLC system equipped with a Xevo G3 QTOF. A ACQUITY UPLC BEH C18 Column, 130Å, 1.7 µm, 2.1 mm X 150 mm was used. The mobile Phase A was: 100% distilled water from Avidity Science, Duo System, Type 1 water +0.1% Formic acid (Waters Formic Acid P/N 186006691-1). The mobile phase B: 100% Acetonitrile from Fisher, Optima LC-MS Grade + 0.1% Formic acid (Waters Formic Acid P/N 186006691-1). The flow rate was 0.4ml/min and the injection volume 1uL. Three repeats were performed each time for solutions prepared as follows: 0.65 g of finely grinded citrus peel powder, either from lemon or orange, was suspended in 8 mL with distilled water in a 10 mL microwave tube and the pH adjusted to coincide with the pH of the synthesis solution as determined experimentally. The suspension was irradiated at 68 °C for 11 minutes under continuous stirring using a CEM Discover SP Microwave Reactor. The suspension was then pre-filtered through a 0.2 um PTFE filter, before the solution being injected in the LC-MS.
X-ray photoelectron spectroscopy (XPS) analysis was performed on a PHI VersaProbe II (Physical Electronics) equipped with an Al Kα X-ray source (1486.6 eV) to determine the surface chemical composition of the samples. Table 6 summarises XPS fittings.

Table 6: Summary of C1s XPS Fitting [a]

C1s (eV)	C1 (284.3)	C2 (285)	C3 (286.2)	C4 (288.9)
LS/ FWHM	DS(0.1,450)/ 1	DS(0.05,450)/ 1.2	GL(30))/ 1.7	GL(30))/ 1.7

Author contributions

R. A. and S. A. conceived and supervised the study. FDL and PD performed electrocatalytic test and IN synthesised the electrocatalysts. FDL and AS performed materials characterization, whereas RA contributed the analysis of the XPS data. CI performed TEM measurements. RA and FDL drafted the manuscript. All the authors contributed revision and finalization of the manuscript.

Acknowledgments

R. A. wish to acknowledge Lee Harman and Paulina Kalinowska at the University of Salford for performing LC-MS analysis.

Conflicts of interest

There are no conflicts to declare.

Data availability

Data for this article are available at salford-repository.worktribe.com

Notes and references

1. S. Ye, M. Hall, H. Cao, P. He, Degradation Resistant Cathodes in Polymer Electrolyte Membrane Fuel Cells. *ECS Transactions* 2016, **3**, 657–666.
2. R. Arrigo, T. Sasaki, J. Callison, D. Gianolio, M. E. Schuster, Monitoring dynamics of defects and single Fe atoms in N-functionalized few-layer graphene by in situ temperature programmed scanning transmission electron microscopy. *Journal of Energy Chemistry* 2021, **64**, 520–530.
3 O. A. Baturina, Q. Lu, A. Purdy, F. Xu, B. Dyatkin, X. Sang, R. Unocic, T. Brintlinger, Y. Gogotsi, Effect of Nanostructured Carbon Support on Copper Electrocatalytic Activity toward CO_2 Electroreduction to Hydrocarbon Fuels. *Catalysis Today* 2017, **288**, 2–10.
4 O. A. Baturina, Q. Lu, M. A. Padilla, L. Xin, W. Li, A. Serov, K. Artyushkova, P. Atanassov, F. Xu, A. Epshteyn, T. Brintlinger, M. Schuette, G. E. Collins, CO_2 Electroreduction to Hydrocarbons on Carbon-Supported Cu Nanoparticles. *ACS Catalysis,* 2014, **4**, 3682–3695.
5 N. Gutiérrez-Guerra, L. Moreno-López, J. C. Serrano-Ruiz, J. L. Valverde, A. de Lucas-Consuegra, Gas Phase Electrocatalytic Conversion of CO_2 to Syn-Fuels on Cu Based Catalysts-Electrodes. *Applied Catalysis B: Environmental*, 2016, **188**, 272–282.
6 J. Masa, W. Xia, M. Muhler, W. Schuhmann, On the Role of Metals in Nitrogen-Doped Carbon Electrocatalysts for Oxygen Reduction, *Angewandte Chemie International Edition,* 2015, **54**, 10102–10120.
7 G. L. Chai, Z. X. Guo, Highly Effective Sites and Selectivity of Nitrogen-Doped Graphene/CNT Catalysts for CO_2 Electrochemical Reduction, *Chemical Science,* 2016, **7**, 1268–1275.
8 Q. Li, W. Zhu, J. Fu, H. Zhang, G. Wu, S. Sun, Controlled Assembly of Cu Nanoparticles on Pyridinic-N Rich Graphene for Electrochemical Reduction of CO_2 to Ethylene, *Nano Energy,* 2016, **24**, 1–9.
9 J., Wu, R. M., Yadav, M., Liu, P. P., Sharma, C. S., Tiwary, L., Ma, X. Zou, X. Zhou, B. I. Yakobson, J. Lou, P. M. Ajayan, Achieving Highly Efficient, Selective, and Stable CO_2 Reduction on Nitrogen-Doped Carbon Nanotubes, *ACS Nano*, 2015, **5**, 5364–5371.
10 Y. Lum, Y. Kwon, P. Lobaccaro, L. Chen, E. L. Clark, A. T. Bell, J. W. Ager, Trace Levels of Copper in Carbon Materials Show

View Article Online
DOI: 10.1039/D4SU00463A

Significant Electrochemical CO_2 Reduction Activity, *ACS Catalysis,* 2016, **6**, 202–209.
11 M. M. Titirici, et al., Sustainable carbon materials. *Chemical Society Reviews, 2015,* **44**, 250–290.
12 M. W. Thielke, G. Tian, & J, Sobrido, Sustainable electrodes for the next generation of redox flow batteries, *JPhys Materials,* 2022, **5**.
13. The World Counts. Wasted Food Statistics. The World Counts, 2023.
14. A. Budai, et al., Biochar Carbon Stability Test Method: An assessment of methods to determine biochar carbon stability, *International Biochar Initiative, 2013,* 1–10.
15. T. Miah, et al., Orange Peel Biomass-derived Carbon Supported Cu Electrocatalysts Active in the CO_2-Reduction to Formic Acid, *ChemPhysChem, 2023,* 202200589.
16. A. Loiudice, et al., Tailoring Copper Nanocrystals towards C_2 Products in Electrochemical CO_2 Reduction, *Angewandte Chemie, 2016,* **128**, 5883–5886.
17. B. C. Marepally, et al., Electrocatalytic reduction of CO_2 over dendritic-type Cu-A and Fe-based electrodes prepared by electrodeposition, *Journal of CO_2 Utilization, 2020,* **35**, 194–204.
18. G. A. Tompsett, C. Conner, K. S. Yngvesson, Microwave Synthesis of Nanoporous Materials, *ChemPhysChem, 2006,* **7**, 296–319.
19. R. Arrigo, M.E. Schuster, On the High Structural Heterogeneity of Fe-Impregnated Graphitic-Carbon Catalysts from Fe Nitrate Precursor, *Catalysts, 2019,* **9**, 303.
20. A.I. Large, S. Wahl, S. Abate, I. da Silva, J.J. Delgado Jaen, N. Pinna, G. Held, R. Arrigo, Investigations of Carbon Nitride-Supported Mn_3O_4 Oxide Nanoparticles for ORR. *Catalysts, 2020,* **10**, 1289.
21. B. Kumar, et al., Nanohybrid Cu@C: synthesis, characterization and application in enhancement of lubricity. *Composite Interfaces, 2020,* **27**, 777–794.
22. R. Arrigo, et al., Influence of Synthesis Conditions on the Structure of Nickel Nanoparticles and their Reactivity in Selective Asymmetric Hydrogenation, *ChemCatChem*, 2020, **12**, 1491-1503.
23. T. Ghodselahi, M. A. Vesaghi, A. Shafiekhani, A. Baghizadeh, M. Lameii, XPS study of the Cu@Cu_2O core-shell nanoparticles. *Applied Surface Science,* 2008, **255**, 2730–2734.
24. M. T. Greiner, *et al*., The oxidation of copper catalysts during ethylene epoxidation, *Phys. Chem. Chem. Phys., 2015,* **17**, 25073-25089.
25. R. Arrigo, et al., Tuning the acid/base properties of nanocarbons by functionalization via amination, *Journal of the American Chemical Society, 2010,* **132**, 9616–9630.
26. R. Arrigo, et al., Dynamics at Polarized Carbon Dioxide–Iron Oxyhydroxide Interfaces Unveil the Origin of Multicarbon Product Formation, *ACS Catalysis 2022,* **12**, 411–430.
27. R. Arrigo, et al., Dynamics over a Cu–graphite electrode during the gas-phase CO_2 reduction investigated by APXPS, *Faraday Discuss., 2022,* **236**, 126-140.
28. V. Kuzmenko, et al., Cellulose-derived carbon nanofibers/graphene composite electrodes for powerful compact supercapacitors. *RSC Advances 2017,* **7**, 45968–45977.
29. G. Nieto, *et al*., Valorization of Citrus Co-Products: Recovery of Bioactive Compounds and Application in Meat and Meat Products, *Plants*, 2021, **10**, 1069.
30. J. Qiao, Y. Liu, F. Hong, J. Zhang, A review of catalysts for the electroreduction of carbon dioxide to produce low-carbon fuels, *Chemical Society Reviews, 2014,* **43**.
31. P. Connor, J. Schuch, B. Kaiser, W. Jaegermann, The Determination of Electrochemical Active Surface Area and Specific Capacity Revisited for the System MnOx as an Oxygen Evolution Catalyst, *Zeitschrift fur Physikalische Chemie, 2020,* **234**, 979–994.
32. X. Liu, et al., Structural disorder determines capacitance in nanoporous carbons, *Science, 2024,* **384**, 321-325.
33. C. J. Bondue, M. Graf, A. Goyal, M. T. M. Koper, Suppression of Hydrogen Evolution in Acidic Electrolytes by Electrochemical CO_2 Reduction, *Journal of the American Chemical Society, 2021,* **143**, 279–285.
34. M. E. Leonard, L. E. Clarke, A. Forner-Cuenca, S. M. Brown, F. R. Brushett, Investigating Electrode Flooding in a Flowing Electrolyte, Gas-Fed Carbon Dioxide Electrolyzer, *ChemSusChem* 2020, **13**, 400–411.
35. a) F. P. Abramo, et al., Electrocatalytic production of glycolic acid via oxalic acid reduction on titania debris supported on a TiO_2 nanotube array, *Journal of Energy Chemistry, 2021,* **68**, 669–678.; b) F. P. Abramo, et al., Nanostructure-performance relationships in titania-only electrodes for the selective electrocatalytic hydrogenation of oxalic acid, *Journal of Catalysis, 2024,* **429**, 115277.
36. D. Gianolio, M. D. Higham, M. G. Quesne, M. Aramini, R. Xu, A. I. Large, G. Held, J.J. Velasco-Vélez, M. Haevecker, A. Knop-Gericke, C. Genovese, C. Ampelli, M. E. Schuster, S. Perathoner, G. Centi, C. R. A. Catlow, R. Arrigo, *ACS Catalysis*, 2023, **13**, 5876-5895.
37. S. J. Raaijman, N. Arulmozhi, M. T. M. Koper, Morphological Stability of Copper Surfaces under Reducing Conditions, *ACS Appl. Mater. Interfaces, 2021,* **13**, 41, 48730-48744.
38. M. Favaro, H. Xiao, T. Cheng, W. A. Goddard, J. Yano, E. J. Crumlin, Subsurface oxide plays a critical role in CO_2 activation by Cu(111) surfaces to form chemisorbed CO_2, the first step in reduction of CO_2. *Proc. Natl. Acad. Sci. U. S. A.*, 2017, **114**, 6706−6711.
39. G. Liu, M. Lee, S. Kwon, J. Eichhorn, A. K. Bucley, F. D. Toste, W. A. Goddard III, F. M. Toma, CO_2 reduction on pure Cu produces only H_2 after subsurface O is depleted: Theory and experiment, *PNAS, 2021,* **118**, e2012649118.
40. A. Loiudice, P. Lobaccaro, E. A. Kamali, T. Thao, B. H. Huang, J. W. Ager, R. Buonsanti, Tailoring Copper Nanocrystals towards C_2 Products in Electrochemical CO_2 Reduction, *Angew. Chemie Int. Ed.*, 2016, **55**, 5789-5792.
41. X. Feng, K. Jiang, S. Fan, M. W. Kanan, Grain-Boundary-Dependent CO_2 Electroreduction Activity, *J. Am. Chem. Soc.*, 2015, **137**, 4606-4609.
42. A. S. Varela, M. Kroschel, T. Reier, P. Strasser, Controlling the selectivity of CO_2 electroreduction on copper: The effect of the electrolyte concentration and the importance of the local pH, *Catal. Today*, 2016, **260**, 8-13.
43. M. Liu, Y. Pang, B. Zhang, P. De Luna, O. Voznyy, J. Xu, X. Zheng, C. T. Dinh, F. Fan, C. Cao, F. P. García de Arquer, T. S. Safaei, A.Mepham, A. Klinkova, E. Kumacheva, T. Filleter, D. Sinton, S. O. Kelley, E. H. Sargent, Enhanced electrocatalytic CO_2 reduction via field-induced reagent concentration, *Nature*, 2016, 537, 382–386.
44. Y. Zhang, C. Liang, J. Wu, H. Liu, B. Zhang, Z. Jiang, S. Li, P. Xu, Recent Advances in Magnetic Field-Enhanced Electrocatalysis, *ACS Appl. Energy Mater.*, 2020, **3**, 10303–10316.
45. M. Ye, T. Shao, J. Liu, C. Li, B. Song, S. Liu, Phase engineering of Cu@Cu_2O core-shell nanospheres for boosting tandem electrochemical CO_2 reduction to C_{2+} products, *Applied Surface Science, 2023,* **622**, 156981.
46. R. Arrigo, T. Sasaki, J. Callison, D. Gianolio, M.E. Schuster, Monitoring dynamics of defects and single Fe atoms in N-functionalized few-layer graphene by in situ temperature programmed scanning transmission electron microscopy, *Journal of Energy Chemistry, 2022,* **64**, 520.

View Article Online
DOI: 10.1039/D4SU00463A

47. R. Arrigo, et al., Pd Supported on Carbon Nitride Boosts the Direct Hydrogen Peroxide Synthesis. *ACS Catalysis, 2016,* **6**, 6959–6966.
48. C. Jimenez, et al., Effect of carbon support on the catalytic activity of copper-based catalyst in CO_2 electroreduction, *Separation and Purification Technology, 2020,* **248**, 1170831.
49. X. Li, et al., Titanium dioxide nanotubes as model systems for electrosorption studies. *Nanomaterials, 2018,* **8**.
50. J. Qiao, P. Jiang, J. Liu, J. Zhang, Formation of Cu nanostructured electrode surfaces by an annealing-electroreduction procedure to achieve high-efficiency CO_2 electroreduction, *Electrochemistry Communications, 2014,* **38**, 8–11.
51. L. de Sousa, C. Harmoko, N. Benes, G. Mul, Optimizing the Ink Formulation for Preparation of Cu-Based Gas Diffusion Electrodes Yielding Ethylene in Electroreduction of CO_2. *ACS ES&T Engineering, 2021,* **1**, 1649–1658.

View Article Online
DOI: 10.1039/D4SU00463A

Data availability Statement

Data for this article are available at salford-repository.worktribe.com